Nanoscale

Evolution map of the memristor: from capacitive state to resistive switching state†

Journal:	*Nanoscale*
Manuscript ID	NR-COM-07-2019-005550.R2
Article Type:	Communication
Date Submitted by the Author:	23-Aug-2019

Complete List of Authors:	Duan, Shukai; Southwest University, College of Electronic and Information Engineering; Zhou, Guangdong; Southwest University, Facuty of materials and energy Wu, Jinggao; Southwest University Wang, Lidan; Southwest University Sun, Bai; Southwest Jiaotong University, Ren, Zhijun; Southwest University, Facuty of materials and energy Xu, Cunyun; Southwest University Yao, Yan Qing; Southwest University Liao, Liping ; Southwest University, College of Electronic and Information Engineering Wang, Gang; Southwest University, College of Electronic and Information Engineering Zheng, Shaohui; Southwest University Mazumder, Pinaki ; University of Michigan, Department of Electrical Engineering and Computer Science Song, Qun Liang; Southwest University

ARTICLE

Evolution map of the memristor: from pure capacitive state to resistive switching state†

Received 00th January 20xx,
Accepted 00th January 20xx

DOI: 10.1039/x0xx00000x

Guangdong Zhou, ‡[a] Jinggao Wu, ‡[a] Lidan Wang, ‡[a] Bai Sun, ‡[b] Zhijun Ren, ‡[a] Cunyun Xu, [a] Yanqing Yao, [a] Liping Liao, [a] Gang Wang, [a] Shaohui Zheng, [a] Pinaki Mazumder, *[c] Shukai Duan *[a] and Qunliang Song *[a]

Memristor has presented great application prospects in terabit nonvolatile storage devices, memory-in-logic algorithmic chips and bio-inspired artificial neural network systems. However, "what is the origin state of the memristor?" is still the basic question for a half of century, especially, while people operate these applications using the memristor, the origin term becomes the fundamental issue. We reveal a new state, pure capacitance state (PCS), which occurs before the memristor triggered, as the origin state of the memristor is verifed in the memory cells through controlling the ambience parameter. Discovery of the PCS, a missing earlier stage in the memristor, finishes the whole evolution map of the memristor from the very beginning to the final developed state.

Introduction

Capacitive device has shown its great potential and advantage in the electronic devices. [1] For instance, touch sensor, [2, 3] energy storage [4, 5] and high performance transistor [6, 7] could be developed using a capacitive behavior. Therefore, the behavior has been particularly focused once it is discovered in any electronic devices.

Memristor envisages making inroads into a wide array of Boolean and non-Boolean applications, ranging from terabit nonvolatile storage devices, memory-in-logic algorithmic chips, and bio-inspired artificial neural network systems. [8-17] Very important, the hardware implementation of neuromorphic computing has been developed using the capacitive behavior observed in the memristor. [18-20] The capacitive feature presented today has been believed to be a unique stage of the memristor. [21, 22]

However, "what is the origin state of the memristor?" is a fundamental question while operating applications. Memristor is normally believed being evolved from a physical reconfiguration (either ions or/and electrons) of the switching function material step by step. [23-27] A redox capacitance state (RCS) as an initial state of the memristor possibly appears before the physical reconfiguration triggered. [28-31]

However, our previous work has demonstrated that the RCS is easily submerged by a high current density due to the formation of conduction paths. [31] In other words, the RCS is easily submerged by the RS state. I. Valov and J. L. M. Rupp groups have emphasized that the moisture-induced redox reactions at interfaces/surfaces play a dominated role in the RCS observation. [32-34] If we want to grasp the evolving process of the memristor, these reactions have to be well controlled.

Nanobelts, nanorods and nanowires as promising function blocks have been extensively investigated in a large number of electronic devices due to their bottom-up growth. [35] For instance, the MoO_3 nanobelt with the high concentration active surface is sensitive to an external environment (i.e., moisture). [36] Therefore, the MoO_3 nanobelt with a large concentration of exposed active surfaces possibly makes the redox reaction control feasible.

In this work, the MoO_3 nanobelt-based lateral device is deliberately designed to study the evolution process of the memristor. Based on theoretical calculations, a physical model is proposed to understand the evolving processes.

Results and discussion

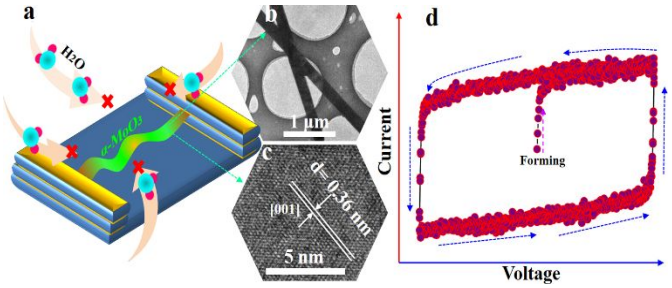

Fig. 1 (a) Schematic of single crystal α-MoO_3 nanobelt-based lateral device under dry ambient. HR-TEM image of (b) the nanobelt structure and (c) the lattice plane of [001]. (d) The pure capacitance state (PCS) observation under dry ambient with the RH of 0%.

[a] School of Mathematic and Statistic; School of Materials and Energy; College of Electronic and Information Engineering; School of Artificial Intelligence; Southwest University, Chongqing, 400715. China.
[b] School of Physical Science and Technology, Southwest Jiaotong University, Chengdu 610031, China.
[c] Department of Electrical Engineering and Computer Science, University of Michigan, 48109, United States.
‡ Authors equally contribute to this work.
*Corresponding Authors email: pinakimazum@gmail.com; duansk@swu.edu.cn; qlsong@swu.edu.cn

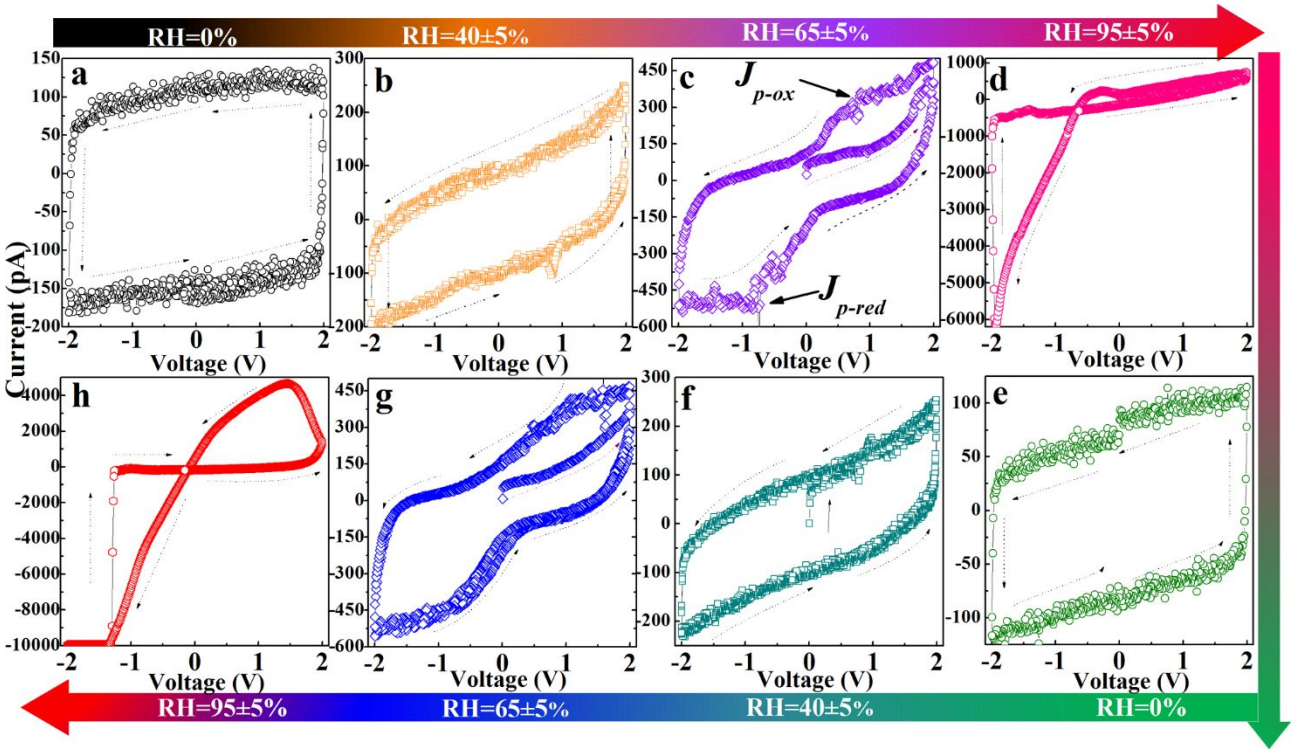

Fig. 2 (a) PCS is observed in an ultralong MoO_3 nanobelt-based device under the RH of 0%. (b) An enhanced PCS under air ambient with the RH of 40%±5%. (c) RCS under the RH of 65%±5%. (d) RS state under the RH of 95%±5%. (e)~(h) The PCS, enhanced-PCS, RCS and RS state are re-observed when reversing the RH level from 0% to 40%±5%, 65%±5% and 95%±5%, respectively.

Figure 1a is a schematic diagram of Ag|α-MoO_3|Ag device with a lateral structure, in which the H_2O adsorption and reaction are throughly restricted. The nanobelt structure of the MoO_3 has been verified by the high resolution transmission electron microscopy (HR-TEM) image, as shown in Figure 1b. The interplanar distance of 0.36 nm, which is originated from the lattice plane of [100], has been also illustrated by an enlarged HR-TEM image, as shown in Figure 1c. It should be pointed out that a single crystal structure of the MoO_3 nanobelt can be also verified by its corresponding selected-area diffraction patterns (data not shown here).

F. M. Messerschmitt and E. Sediva have stressed that the H_2O-based redox reactions at the interfaces and surfaces are possible the reason for the RCS behaviors. [37, 38] To be noted that a pure capacitance state (PCS) has been impressively discovered in the Ag|α-MoO_3 nanobelt|Ag device when the H_2O-based reaction is throughly removed (Figure 1d).

Compliance current (CC) dependent of the PCS has been investigated. One can see that the PCS can be maintained under the CC level of 100 and 10 nA, but it is seriously limited when the CC decreases to 0.1 nA, as shown in **Figure S1a**. Therefore, to obeserve the PCS, a suitable CC level is needed. In addition, bias voltage magnitude dependency of the PCS illustrates that the PCS has a satuation current value at 3 V, as shown in Figure S1b. Namely, the PCS will reach its maxmum charge storage capability when the bias voltage overs 3 V. The PCS are well maintained after operating consecutive *I-V* hystersis for 500 cycles at room temperature, as shown in Figure S1c. It implys that the PCS has good cycling endurance.

To be noted that a constant bias voltage sweep rate of 1.0 V/s is employed during the PCS measurements. The PCS has also shown good endurance for the bias volatge sweep rate (data not shown here). In fact, our previous works had demonstrated that the film-based device was sensitive to the bias voltage sweep rate, but the ultralong nanobelt or nanorod-based device shown good endurance for the high bias scan rate. [39, 40] In other words, Interface-induced *I-V* hysteresis is efficiently modulated by the bias voltage sweep rate.

Since the RCS appearance is strongly depended on the moisture level, a series of influences from the H_2O have to be further investigated. It is worth noting that the Ag|MoO_3|Ag device is exposed from the RH of 0% into the high RH of 95%, the PCS disappears, but the RS state is observed, as shown in Figure S1d. Therefore, we have deduced that the PCS, RCS and RS state are the evolving stages of the memristor.

By further investigation the influence of the H_2O on the PCS, various RH levels (0%, 40%±5%, 65%±5% and 95%±5%) are artificially synthesized in our laboratory. The cyclic voltammetry measurements operated on the Ag|MoO_3|Ag device in dry air with RH of 0% exhibit the PCS behavior (**Figure 2a**). When the device is exposed to the air atmosphere with the RH of 40%±5% for 30 minutes, the PCS behavior is well maintained, but it has a high current value (Figure 2b). It indicates that an enhanced PCS can be induced by appropriate H_2O concentration. Here, the strong PCS is defined to be an enhanced-PCS. The RH levels are elevated from the 40%±5% to 65%±5%, the H_2O-based redox reaction expectedly occurs, which leads to the RCS emerging (Figure 2c).

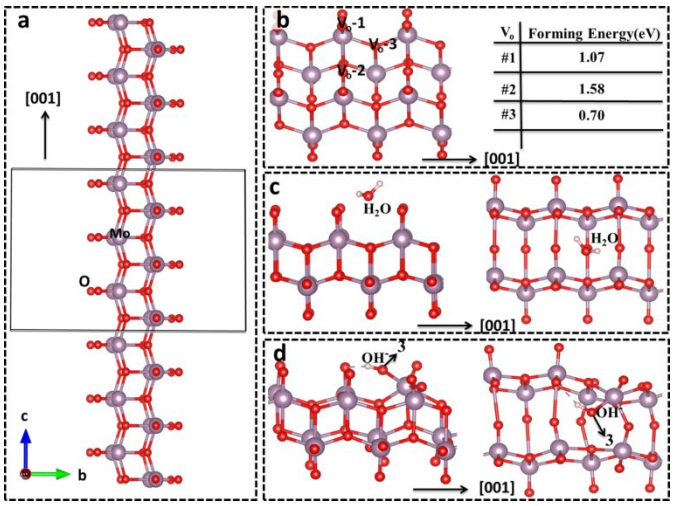

Fig.3 First principle calculation on formation energy of oxygen vacancy (V_o) and H_2O molecule splitting on the surface of the MoO_3 nanobelt. (a) Single crystal MoO_3 nanobelt extended in the lattice direction of [001]. (b) The formation energy for the possible surface V_o sites V_{o-1},V_{o-2}, V_{o-3} are 1.07, 1.58 and 0.70 eV, respectively. (c) H_2O molecule adsorption process is described when the MoO_3 nanobelt is exposed into a moisture ambient. (d) The OH^- ions are generated by H_2O-based redox reaction.

When the device is exposed to the RH of 95%±5%, the RS state characterized by a bipolar resistive switching memory is observed (Figure 2d). It is worth noting that the observed RS state does not cross at the zero bias voltage, but crossing at negative bias voltage, indicating there are negative polarized charges in the host MoO_3 or interfaces. To study the PCS reversibility, the RH level is sharply decreased from nearly 100% to 0%, and the PCS appears again. Subsequently, as RH gradually increases from 0% to 40%±5%, 65%±5% and 95%±5%, the enhanced PCS, RCS and the RS state are re-observed (Figures 2e-2h).

Above experiments can be sumarized as six points:

i) PCS only can be detected under dry ambient (RH=0%);

ii)Enhanced-PCS appears after exposing the device from dry ambient to moisture ambient (RH= 40%±5%);

iii)RCS characterized by the redox peaks is observed after increasing the moisture level from the RH of 40%±5% to 65%±5%.

iv)RS as the final state is observed when the RH of 65%±5% consecutively elevates to the 95%±5%.

v) Current density shows a consecutive increase tendency from PCS, enhanced-PCS, RCS and RS state, respectively.

vi)H_2O adsorption and redox reaction at the surfaces outwigh the adsorption and reaction at the intefaces.

Y. Li and Y. Gao have reported that the H_2O-based redox reactions take place at the active surface/subsurface oxygen vacancy (V_o).[41] Therefore, the active surface V_o sites should be considered for the MoO_3 nanobelt. Since the surface V_o in MoO_3 nanobelt plays the dominant role in H_2O-related reactions, the active V_o with the lowest forming energy is needed to figure out.

Based on the constructed MoO_3 super-cell along the [001] direction (**Figure 3a**), the V_o can be classified into three groups: V_{o-1}, V_{o-2} and V_{o-3} site, as shown in Figure 3b. Our DFT calculation results demonstrate that the formation energy for V_{o-1}, V_{o-2} and V_{o-3} site is 1.07, 1.58 and 0.70 eV. Therefore, the H_2O adsorbed at the surface of the MoO_3 nanobelt firstly reacts with the surface V_{o-3} due to its lowest formation energy. Figure 3c denotes the H_2Omolecules adsorption on the surface of MoO_3 nanobelt. After that, the OH^- ions are generated due to the H_2O molecules react with the surface V_{o-3}, as shown in Figure 3d.

It is worth noting that the electric conductivity, which is dominated by the energy band structure of the materias, is gradually enhanced from the PCS to RS state. Thus, the influence from the H_2O adsorption, redox reaction and ion migraton on the energy band structure has to be verified.

Projected density of states (PDOS) *versus* energy demonstrate the bulk MoO_3 with an energy gap (E_g)1.75 eV of 1.75 eV (**Figure 4a**), which is consistent with previous results.[42, 43] Thus, physical model in this work is reasonable. When MoO_3 nanobelt has not adsorbed the H_2O molecules, the DOS *versus* energy result shows a 3.16 eV of the E_g, which is larger than the bulk MoO_3, as shown in Figure 4b. Fermi energy level approaches to the valence band for both the MoO_3 bulk and nanobelt under the dry ambient (RH=0%), showing a p-type feature. The Fermi energy level has shifted its position from the valence band to the conduction band when H_2O is absorbed on the surface of MoO_3 nanobelt, leading to both p- and n-type characterics, as shown in Figure 4c. After OH^- ion, which is originated from H_2O-based redox reactions, hangs on the surface of the MoO_3 nanobelt resulting in the E_g decreasing from 3.32 to 3.02 eV and Fermi energy level shifting

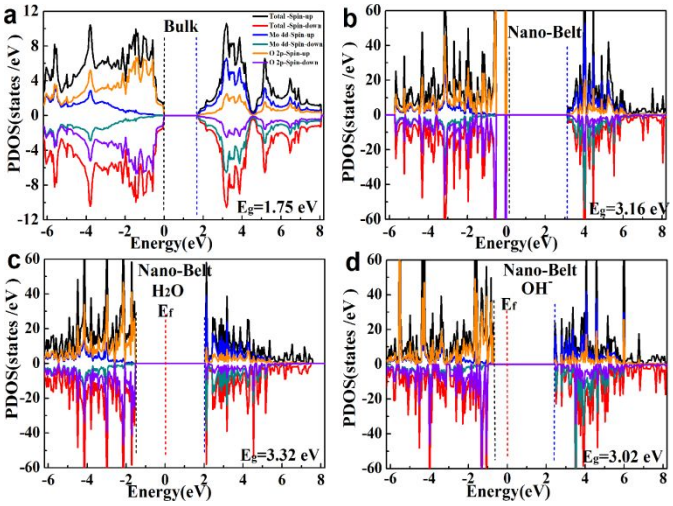

Fig. 4 (a) Projected density of states (PDOS) of Mo and O atoms of MoO_3 bulk materials, where the band gap energy (E_g) is 1.75 eV. (b) PDOS of Mo and O atoms of the MoO_3 nanobelt, where the E_g is 3.16 eV. The Fermi energy level is close to the valence band, which implies that MoO_3 is p-type. The band structure of the MoO_3 nanobelt (c) after adsorbing H_2O molecule and (d) suspending OH^- ions due to the H_2O-based redox reactions.

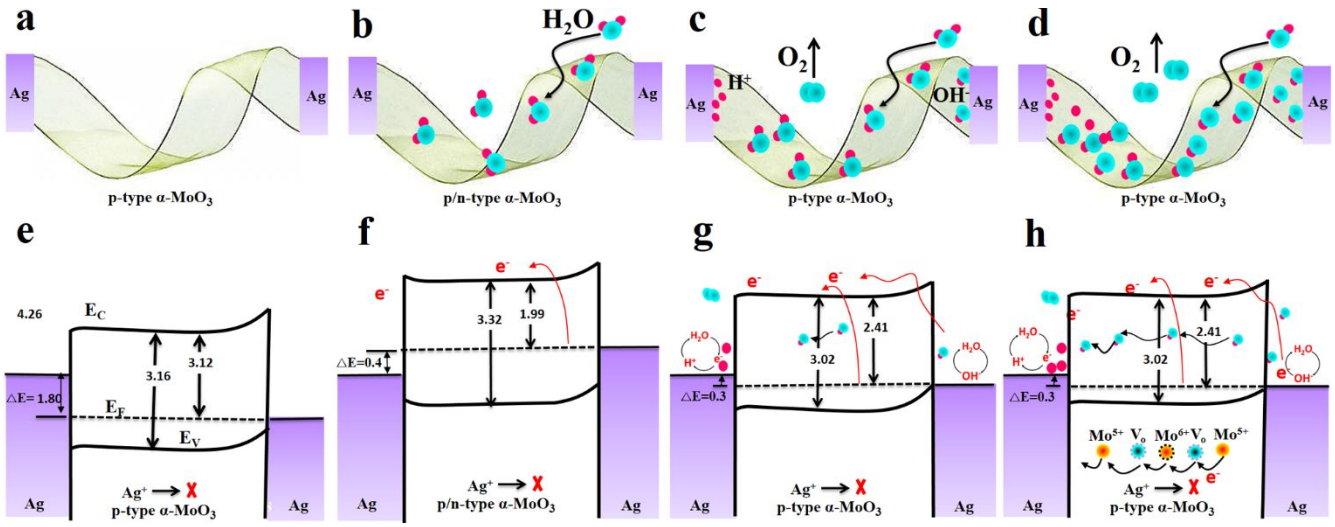

Fig. 5 Energy band structure model for the PCS, enhanced-PCS, RCS and RS state under different moisture level. Schematic of the Ag|α-MoO_3|Ag device under (a) the dry ambient (the PCS), (b) after adsorption H_2O molecules on the surface of MoO_3 nanobelt (enhanced PCS), (c) OH^- ion suspending on the surface due to the H_2O redox reactions (RCS) and (d) Electron transfer and ion migration along the surface of MoO_3 nanobelt (RS state).

to the side of the valence band again, as shown in Figure 4d.

Conclusion on the theoretical calculations can be drawn as following points:

i) Active surface $V_{o\text{-}3}$ is verified.

ii) H_2O after adsorbing on the surface of MoO_3 nanobelt and firstly react with the surface $V_{o\text{-}3}$.

iii) Band gap of the E_g and the Fermi energy level of the MoO_3 nanobelt are efficiently modulated by the H_2O adsorption and redox reaction.

Based on the experimental observations and theoretical calculations, the explanation for the PCS, enhanced-PCS, RCS and RS state can be made. Before making the explanation for the above states, there are three points need to elaborate.

Firstly, the Ag^+ ion-based conductive filament is seriously restricted due to the ultralong scale of the MoO_3 nanobelt. To further verify the effect of Ag^+, the EDX spectra are operated on the Ag|MoO_3|Ag device during the different stages of bias volatge sweep, as shown in **Figure S2a**. The length of the MoO_3 nanobelt is ~ 65 μm, as shown in Figure S2b. To be noted that the Ag signal has shown a negilible variation during the bias voltage sweep. This has been verified by our previous work as well. [39, 40, 44]

Secondly, the Mo and O signals also show an negligible variation. Therefore, the Mo^{x+} -base migration is not the main factor considered during the evolving process.

Thirdly, the ions in the oxygen species deficient region ($O_{x\,ads}^{-}$) can field-driven migrate and contribute to the electric conductivity, but it is negligible due to its low concentration on the surface. [40, 45, 46]

Figures 5a-5d are the schematic diagram for the Ag|MoO_3|Ag device under the dry ambient, adsorption of H_2O molecule, H_2O-related redox process and OH^- ion-induced conduction filament formation, respectively.

Due to the existence of the metal-oxide contact, there is a 1.8 eV potential between the Ag and the Fermi energy level of the MoO_3 nanobelt, which makes the hole transport becomes much more difficult, as shown in Figure 5e. In addition, the redox reactions at the surfaces and interfaces are restrained under the RH of 0%. In this case, the interplay between ions and electrons, electron transfer and ion migraton are seriously limited. The field-driven electrons are accumulated on the both ends of the MoO_3 nanobelt. Therefore, the Ag|MoO_3|Ag device corresponds to a capacitor, that is why the device only presents the PCS behaviors under dry ambient.

After exposing our device from the RH of 0% to 40%±5%, the Fermi energy level shifts its position to the side of valence band, simultaneously, the potential of the metal-oxide decreases from 1.8 to 0.4 eV, as shown in Figure 5f. The electrons surrounded the H_2O will transfer to the surface of the MoO_3 nanobelt. In addition, the electrons at impurity energy levels possibly transfer to the valence band due to the low distance between Fermi energy level and bottom of the valence band (decreasing from 3.12 to 1.99 eV). In this case, an enhanced PCS would be observed.

As for the RCS, the H_2O firstly adsorbs on the surface of MoO_3 nanobelt and then reacts with the surface $V_{o\text{-}3}$. This redox process results in the E_g decreasing from 3.32 to 3.02 eV and the potential of metal-oxide contact decreasing from 0.4 to 0.3 eV, as shown in Figure 5g.

The RCS is described by the Randles-Sevcik equation: [47]

$$J_p = 2.99 \times 10^5 \times z^{3/2} \times C_{redox} \times \sqrt{\partial D_{redox} \nu} \qquad (1)$$

where the J_p, z, C_{redox}, α, D_{redox}, ν denote the redox (oxidization or reduction) peak current density, the number of electrons transfer during redox reaction, the concentration of ions, the charge transfer coefficient, the ion diffusion coefficient, and the bias voltage sweep rate, respectively. By the Eq. (1), the RCS is determined by bias sweep rate, ion concentration and diffusion coefficient and the number of electrons transferred. Namely, a large number of OH^- ions, which are generated by

the interaction of the H_2O molecule with the surface V_o, are suspended at the surface of the MoO_3 nanobelt.

The generated OH^- ion can be described as following: [48-50]

$$H_2O + O_O^{\times} + V_o \rightleftarrows 2OH^- \quad (2)$$

where the O_o^X, V_o denote the oxygen atom in lattice and intrinsic oxygen vacancies, respectively. According to half-cell theory, the H_2O-based chemical reactions possibly take place at the interface of our device, which are described as following: [51, 52]

$$2H_2O \rightleftarrows O_2\uparrow + 4H^+ + 4e^- \quad (3)$$

$$O_2 + 2H_2O + 4e^- \rightleftarrows 4OH^- \quad (4)$$

For a film-based device, the *I-V* hysteresis is dominated by these reactions at the interface. Different from the film-based device, the RCS is mainly dominated by the H_2O-based redox reaction at the surface of the MoO_3 nanobelt. Taking into acount the high concentration of the surface V_o, the OH^- ions are contributed by the Eq. (2) more than the Eq. (3) and Eq. (4). The generation of OH^- ions suspending on the surface of the MoO_3 nanobelt leads to a downscaling of E_g. In this case, the electrons generated from the Eq. (2) and the electrons hopping from impurity energy level to conduction band will directly contribute to the current density of our device. Therefore, the RCS characterized by the redox peaks is observed under the moisture level (RH=65%±5%).

To be noted that OH^- ions are generated as the H_2O-based redox reaction going, simultaneously, the surface V_o is gradually consumed.[53-63] Therefore, a large number of OH^- ions are suspending on the surface of MoO_3 nanobelt. The OH^- ions can migrate along the surface to form a filament-like conduction path and the strong interplay between the ions and electrons simultaneously occurs. The two factors co-drive the device into the RS state, as shown in Figure 5h. The OH^- filament-like path formed at the surface is easily disturbed by external factors, thus, the induced RS state is very unstable.

Not only the RS state is not crossing at 0 V, but also shows an asymmetry in positive and negative bias region. The polarized charges redistribute at the interfaces and nonuniform distribution of the surface V_o are possibly responsible for the asymmetry and nonzero bias crossing RS behaviors. [64-66] Memristor presented today with lateral or vertical structure has shown its great potential applications ranged from natural language processing, object recognition, humanoid robot and data storage.[67-74] The PCS is easily submerged by high current density, for that, the MoO_3 lateral is deliberately designed. It should be pointed out that the PCS, enhanced-PCS, RCS and RS can be aloso detected in the vertical structure of Ag|MoO_3(30nm)|Au memirstor arrays (data not shown here). The evolution process and corresponding physical mechanism are needed to further investiagted in near future.

Conclusion

We reveal a novel charge storage state in the form of pure capacitance state (PCS), a missing earlier phase of memristor, for that, the whole evolution map of memristor is completed. Through controlling the ambience parameter, the PCS, which is submerged by high current density, is found. The evolution map construction provides an avenue for a smart electronic device design such as algorithmic logic-in-memory and bio-inspired neuromorphic computing system.

Experimental Section

Device Fabrication. The 0.005 mol $Ni(NO_3)_2{\cdot}6H_2O$ and 0.005 mol $(NH_4)_6Mo_7{\cdot}4H_2O$ were mixed and dissolved in 30 mL deionized water at room temperature. The mixed solution was continuously stirred for 12 hours at room temperature. After that, 0.03 g hexadecyl trimethyl ammonium bromide was added into the mixed solution, followed by continuous stirring for 3 hours at room temperature. The fabricated solution was transferred into a Teflon-lined steel autoclave, and heated at 500 K for 24 hours. The composites contained the $NiMoO_4$ debris and ultra-long MoO_3 nanobelts were obtained after using the reaction solution centrifuged at 6000 rpm for 10 minutes at room temperature. The centrifuged composites were annealed at 900 K in Argon gas ambient for 8 hours. The precursor solution was obtained using the 0.001g thermal processed composites added into 20 mL deionized water. The precursor solution was spin-coated on the SiO_2 substrate at 8000 rpm for 60 seconds. The single ultra-long MoO_3 was horizontally placed between the two pre-deposited Ag electrodes with 50 μm gap on the SiO_2/Si substrate, and then the Ag paste was dropped on both ends of the ultralong nanobelt. Therefore, the Ag|MoO_3|Ag lateral structure device is developed.

Current *versus* Voltage Hysteresis Measurement. Electrical properties were measured at room temperature in the use of an integrated electric test system including the electrochemical workstation (CHI 660D) and multifunction probe station (Lake Shore TTPX). The air ambient of laboratory with RH of 35%~45% was employed in this work. Dry air (H_2O < 5 ppm) was synthesized by flowing air into three interconnected heated-glass delivery tubes filled with dry CaO powers. The dry air was slowly injected into a test-cavity of the probe station, which was pumped to a high vacuum (5×10^{-4} Pa) until the pressure reaching a balance with outside. Moisture air was synthesized by flowing laboratory air into a gas-washing bottle filled with deionized water. The RH level of the test-cavity was relied on the injection time and rate of moisture air. All of substrate used in this work was clean by Air plasma cleaner (PDC-32G-2) for 30 seconds.

Computational details. The spin-polarized density-functional theory (DFT) calculations in our work were performed using the Vienna abinitio simulation package (VASP).[42] The projector augmented wave (PAW) methodwas used to describe the electron-ion interaction, while the Perdew-Burke-Ernzerh of (PBE) functional implementation of the generalized gradient approximation was used to describe the exchange-correlation interactions. Due to the highly anisotropic crystal structure of α-MoO_3, it is more favorable to grow along the [001] direction forming belt-like crystal structures and with the largely exposed {010} surface.[43] Therefore, the nanobelt MoO_3 system used herein along [001]

direction was constructed from a 2 × 1 ×3 α-MoO_3 supercell with a vacuum layer of at least 15 Å along the x and y axis to minimize the undesired interactions between the Grimme DFT-D2 van der Waals corrections are taken into account in the bulk MoO_3 calculation. [43] The *4d* electrons of Mo and *2p* electrons of O are considered as valence electrons. A Hubbard U parameter of 6.3 eV is added to correct the self-interaction for Mo 4d orbital in bulk and nanobelt MoO_3 systems. The k-points meshes were sampled based on the Γ centered Monkhorst-Pack method[11] with a k-point mesh resolution of 2 $\pi \times 0.04$ Å-1 and 2 $\pi \times 0.01$ $Å^{-1}$ for geometric structure optimization and densities of states (DOS) calculations, respectively. The plane wave energy cutoff of 450 eV has been employed in this work. Electronic energies are computed by assuming the self-consistent field (SCF) tolerance of 10^{-5} eV and the force exerted on an atom converges to less than 0.03 eV/Å. To assess the formation of oxygen vacancy on MoO_3 nanobelt, the oxygen vacancy formation energy ($\triangle E_f$) is given by Eq. (5): [75]

$$\Delta \boldsymbol{E_f} = \boldsymbol{E_{vac}} + \frac{\mathbf{1}}{\mathbf{2}}\boldsymbol{E_{O_2}} - \boldsymbol{E_{total}} \quad (5)$$

where $\mathbf{E_{O_2}}$, E_{vac} and E_{total} are eergy of gas phase of O_2, and the energy of MoO_3 nanobelt with and without V_o, respectively. According to Eq. (5), the lower value of the $\triangle E_f$ indicates the more favorable formation for the V_o.

Conflicts of Interest

There are no conflicts to declare.

Acknowledgements

G. D. Zhou is grateful for funding from the Postdoctoral Program for the Innovative Talent Support of Chongqing (CQBX201806). Q. L. Song and S. K. Duan gratefully acknowledge the National Natural Science Foundation of China (Grant Nos. 11774293, 11274256, 61571372, 61672436, 61601376), Fundamental Research Funds for the Central Universities (Grant Nos.XDJK2016A001, XDJK2017A002 , XDJK2017A005), the Program for Innovation Team Building at Institutions of Higher Education in Chongqing (Grant No. CXTDX201601011), Fundamental Science and Advanced Technology Research Foundation of Chongqing (cstc2016jcyjA0547), China Postdoctoral Science Foundation Special Funded (2018T110937) and Chongqing Postdoctoral Science Foundation Special Funded (Xm2017039). P. Mazumder further acknowledges an ECCS grant of the National Science Foundation in USA.

References

1 Z. Wang, M. Rao, J. W. Han, J. Zhang, P. Lin, Y. Li, C. Li, W. Song, S. Asapu, R. Midya, Y. Zhuo, H. Jiang, J. H. Yoon, N. K. Upadhyay, S. Joshi, M. Hu, J. P. Strachan, M. Barnell, Q. Wu, H. Wu, Q. Qiu, R. S. Williams, Q. Xia and J. J. Yang, *Nat. Commun.,* 2018, **9**, 3208.

2 H. Xu, Y. Lv, D. Qiu, Y. Zhou, H. Zeng and Y. Chu, *Nanoscale*, 2019, **11**, 1570-1578.

3 P. Cataldi, S. Dussoni, L. Ceseracciu, M. Maggiali, L. Natale, G. Metta, A. Athanassiou and I. S. Bayer, *Adv. Sci.*, 2018, **5**, 1700587.

4 P. Ratajczaka, M. E. Sussb, F. Kaasikc and F. Béguin, *Energy. Storage. Mater.*, 2019, **16**, 126-145.

5 M. Li, W. Yang, J. Li, M. Feng, W. Li, H. Li and Y. Yu, *Nanoscale*, 2018, **10**, 2218-2225.

6 M. Si, C. J. Su, C. Jiang, N. J. Conrad, H. Zhou, K. D. Maize, G. Qiu, C. T. Wu, A. Shakouri, M. A. Alam and P. D. Ye, *Nat. Nanotechnol.*, 2018. **13**, 24–28.

7 A. Chortos, Z. Bao, *Mater. Today.*, 2014, **17**, 321-331.

8 S. Kumar, J. P. Strachan and R. S. Williams, *Nature*, 2017, **548**, 318-321.

9 G. D. Zhou, Z. Ren, L. Wang, J. Wu, B. Sun, A. Zhou, G. Zhang, S. Zheng, S. K. Duan and Q. L. Song, *Nano Energy*., 2019, **63，** 103793.

10 Z. Wang, S. Joshi, E. S. Sergey, H. Jiang, R. Midya, P. Lin, M. Hu, N. Ge, J. P. Strachan, Z. Li, Q. Wu, M. Barnell, G.-L. Li, H. L. Xin, R. S. Williams, Q. Xia and J. J. Yan, *Nat. Mater.*, 2017, **16**, 101-108.

11 P. Zhang, M. Xia, F. Zhuge, Y. Zhou, Z. Wang, B. Dong, Y. Fu, K.Yang, Y. Li, Y. He, R. H. Scheicher and X. S. Miao, *Nano Lett.*, 2019, **19**, 4279-4286.

12 Y. Li, Y. Zhong, L. Xu, J. Zhang, X. Xu, H. Sun and X. S. Miao, *Sci. Rep.*, 2013, **3**, 1619.

13 L. Sun, Y. Zhang, G. Han, G. Hwang, J. Jiang, B. Joo, K. Watanabe, T. Taniguchi, Y. M. Kim, W. J. Yu, B. S. Kong, R. Zhao and H. Yang, *Nat. Commun.,* 2019, **10**, 3161.

14 L. Sun, Y. Zhang, G. Hwang, J. Jiang, D. Kim, Y. A. Eshete, R. Zhao and H. Yang, *Nano Lett.*, 2018, **18**, 3229-3234.

15 J. Chen, Y. Wu, K. Zhu, F. Sun, C. Guo, X. Wu, G. Cheng and R. Zheng, *Electrochimica Acta*, 2019, **316**, 133-142.

16 F. Rahman, T. Ahmed, S. Walia, E. Mayes, S. Sriram, M. Bhaskaran and S. Balendhran, *Nanoscale*, 2018, **10**, 19711-19719

17 G. D. Zhou, B. Sun, Z. J. Ren, L. D. Wang, C. Y. Xu, B. Wu, P. Li, Y. Q. Yao and S. K. Duan, *Chem. Commun.*, 2019, **55**, 9915-9918.

18 Q. Xia, J. J. Yang, *Nat. Mater.* 2019, **18**, 309-323.

19 C. O. Callaghan, C. G. Rocha, F. Niosi, H. G. Manning, J. J. Boland and M. S. Ferreira, *J. Appl. Phys.*, 2018, **124**, 152118.

20 T. You, L. P. Selvaraj, H. Zeng, W. Luo, N. Du, D. Bürger, I. Skorupa, S. Prucna, A. Lawerenz, T. Mikolajick, O. G. Schmidt and H. Schmidt, *Adv. Electron. Mater.*, 2016, **2**, 1500352.

21 S. Tappertzhofen, I. Valov, T. Tsuruoka, T. Hasegawa, R. Waser and M. Aono, *ACS Nano.,* 2012, **7**, 6396-6402.

22 S. Tappertzhofen, S. Menzel, I. Valov and R. Waser, *Appl. Phys. Lett.*, 2011, **99**, 203103.

23 X. Yang, Y. Fang, Z. Yu, Z. Wang, T. Zhang, M. Yin, M. Lin, Y. Yang, Y. Cai and R. Huang, *Nanoscale*, 2016, **8**, 18897-18904.

24 D. Ding, D. Wang, M. Zhao, J. Lv, H. Jiang, C. Lu and Z. Tang, *Adv. Mater.*, 2017, **29**, 1603444.

25 X. Chen, P. Huang, X. Zhu, S. Zhuang, H. Zhu, J. Fu, A. S. Nissimagoudar, W. Li, X. Zhang, L. Zhou, Y. Wang, Z. Lv, Y. Zhou and S. T. Han, *Nanoscale Horizons*., 2019, **4**, 697-704.

26 M. Zhao, F. Yang, C. Liang, D. Wang, D. Ding, J. Lv, J. Zhang, W. Hu, C. Lu and Z. Tang, *Adv. Funct. Mater.,* 2016, **26**, 5182-5188.

27 R. Zhang, H. Jiang, Z. R. Wang, P. Lin, Y. Zhuo, D. Holcomb and Q. Xia, *Nanoscale*, 2018, **10**, 2721-2726.

28 L. Zheng, B. Sun, Y. Chen, T. Li, S. Mao, S. Zhu and Y. Zhao, *Mater. Today. Chem.*, 2018, **10**, 167-174.

29 B. Sun, T. Guo, G. D. Zhou, S. Ranjan, W. Hou, Y. Hou and Y. Zhao, *J. Colloid. Interface. Sci.*, 2019, **553**, 682-687.
30 J. J. Yang, M. X. Zhang, J. P. Strachan, F. Miao, M. D. Pickett, R. D. Kelley, G. M. Ribeiro and R. S. Williams, *Appl. Phys. Lett.,* 2010, **97**, 232102.
31 G. D. Zhou, X. Yang, L. Xiao, B. Sun and A. Zhou, *Appl. Phys. Lett.,* 2019, **114**, 163506.
32 I. Valov, T. Tsuruoka, *J. Phys. D: Appl. Phys.,* 2018, **51**, 413001.
33 D. Cho, M. Lübben, S. Wiefels, K. Lee and I. Valov, *ACS Appl. Mater. Interfaces.*, 2017, **9**, 19287-19295.
34 F. Messerschmitt, M. Jansen and J. L. M. Rupp, *Adv. Electron. Mater.,* 2018, **4**, 1800282.
35 G. Milano, S. Porro, I. Valov and C. Ricciardi, *Adv. Electron. Mater.*, 2019, 1800909.
36 G. D. Zhou, W. Zhao, X. Ma and A. K. Zhou, *J. Alloys. Compounds.*, 2016, **679**, 47-53.
37 F. M. Messerschmitt, J. L. Kubicek and L. J. M. Rupp, *Adv. Funct. Mater.* 2015, **25**, 5117-5125.
38 E. Sediva, W. J. Bowman, J. C. G. Rosillo and J. L. M. Rupp, *Adv. Electron. Mater.*, 2018, 1800566.
39 G. D. Zhou, B. Sun, Y. Yao, H. Zhang, K. Alameh, B. Ding and Q. L. Song, *Appl. Phys. Lett.*, 2016, **109**, 143904.
40 X. Yang, Z. Ren, F. Pan, B. Wu, P. Li and G. D. Zhou, *J. Alloys. Compounds.*, 2019, **802**, 546-552.
41 Y. Li, Y. Gao, *Phys. Rev. Lett.*, 2014, **112**, 206101.
42 J. P. Perdew, K. Burke and M. Ernzerhof, *Phys. Rev. Lett.*, 1996, **77**, 3865.
43 T. Liang, W. G. Sawyer, S. S. Perry, S. B. Sinnott and S. R. Phillpot, *Phys. Rev. B.*, 2008, **77**, 104105.
44 G. D. Zhou, B. Sun, B. Wu, X.Q. Liu, S. J. Zhang and A. Zhou, *Composite. Structures.*, 2017, **166**, 177-183.
45 J. Park, S. Lee and K. Yong, *Nanotechnology*, 2012, **23**, 385707.
46 G. D. Zhou, Y. Yao, X. Zhao, X. Liu, B. Sun and A. Zhou, *RSC Adv.*, 2016, **6**, 59370-59374.
47 I. Valov, E. Linn, S. Tappertzhofen and R. Waser, *Nat. Commun.*, 2013, **4**, 1771.
48 M. Lübben, S. Wiefels, R. Waser and I. Valov, *Adv. Electron. Mater.*, 2018, 4, 1700458.
49 G. D. Zhou, S. Duan, P. Li, B. Sun, B. Wu, Y. Yao, X. Yang, J. Han, J. Wu, G. Wang, L. Liao, C. Lin, W. Hu, C. Xu, D. Liu, T. Chen, L. Chen, A. Zhou and Q. L. Song, *Adv. Electron. Mater.*, 2018, **4**, 1700567.
50 A. Zaffora, D. Y. Cho, K. S. Lee, F. D. Quarto, R. Waser, M. Santamaria and I. Valov, *Adv. Mater.*, 2017, **29**, 1703357.
51 S. Tappertzhofen, S. Menzel, I. Valov and R. Waser, *Appl. Phys. Lett.*, 2015, **99**, 203103.
52 M. Lübben, P. Karakolis, I. V. O. Sougleridis, P. Normand, P. Dimitrakis and I. Valov, *Adv. Mater.*, 2015, **27**, 6202-6207.
53 Y. Zhai, J. Q. Yang, Y. Zhou, J. Y. Mao, Y. Ren and V. A. L. Roy, *Mater. Horizons.*, 2018, **5**, 641-654.
54 M. Moors, K. K. Adepalli, Q. Lu, A. Wedig, C. Baumer, K. Skaja, B. Arndt, H. L. Tuller, R. Dittmann, R. Waser, B. Yildiz and I. Valov, *ACS Nano*., 2016, **10**, 1481-1492.
55 G. D. Zhou, B. Wu, X. Liu, P. Li, S. Zhang, B. Sun and A. Zhou, *Phys. Chem. Chem. Phys.*, 2016, **18**, 6509-6514.
56 G. D. Zhou, Y. Q. Yao, Z. S. Lu, X. D. Yang, J. J. Han, G. Wang, Q. Liu and Q. L. Song, *Nanotechnology.*, 2017, **28**, 425202.
57 S. Zhu, B. Sun, Y. Chen, L. Tao, H. Zhao, W. Mao and Y. Zhao, *J. Mater. Chem. C*, 2019, **7**, 7593-7600.
58 Y. Xia, B. Sun, H. Wang, G. D. Zhou, X. Kan and Y. Zhang, *Appl. Surf. Sci*., 2017, **426**, 812-816.
59 G. D. Zhou, Z. S. Lu, Y. Q. Yao, G. Wang, X. D. Yang, A. K. Zhou, P. Li, B. F. Ding and Q. L. Song, *J. Appl. Phys.*, 2017, **121**, 155302.
60 J. P. B. Silva, C. A. Marques, J. A. Moreirab and O. Conde, *J. Mater. Chem. C*, 2017, **5**, 10353-10359.
61 G. D. Zhou, B. Sun, A. Zhou and B. Wu, *Curr. Appl. Phys*., 2017, **17**, 235-239.
62 M. Xiao, D. Shen, K. P. Musselman, W. W. Duley and Y. N. Zhou, *Nanoscale*, 2018, **10**, 6069-6079.
63 W. Banerjee, X. Zhang, Q. Luo, H. Lv, Q. Liu, S. Long and M. Liu, *Adv. Electron. Mater.*, 2018, **4**, 1700561.
64 X. L. Shao, L. W. Zhou, K. L. Zhang, S. Yoo and C. S. Hwang, *Nanoscale*, 2015, **7**, 11063-11074.
65 G. D. Zhou, Z. J. Ren, L. D. Wang, B. Sun, S. K. Duan and Q. L. Song, *Mater. Horizons.*, 2019, **DOI**: 10.1039/C9MH00468H.
66 S. Tappertzhofen, H. Mundelein, I. Valov and R. Waser, *Nanoscale*, 2012, **4**, 3040-3043.
67 Z. Wang, S. R. Zhang, L. Zhou, J. Y. Mao, S. T. Han, Y. Ren, J. Q. Yang, Y. Wang, Y. Zhai and Y. Zhou, *Physica Status Solidi*, 2019, **13**, 1970022
68 L. Zhou, J. Mao, Y. Ren, S.T. Han, V.A.L. Roy and Y. Zhou, *Small*, 2018, **14**, 1703126
69 J. M. Yang, E. S. Choi, S. Y. Kim, J. H. Kim, J. H. Park, N. G. Park, *Nanoscale*, 2019,**11**, 6453-6461
70 Y. Wang Z. Lv, Q. Liao, H. Shan, J. Chen, Y. Zhou, L. Zhou, X. Chen, V. A. L. Roy, Z. Wang, Z. Xu, Y. J. Zeng and S. T. Han, *Adv. Mater.*, 2018, **30**, 1800327.
71 L. Zhou, S. Yang, G. Ding, J. Q. Yang, Y. Ren, S. R. Zhang, J. Y. Mao, Y. Yang, Y. Zhou and S. T. Han, *Nano Energy.,* 2019, **58**, 293-303.
72 B. Sun, Y. Chen, M. Xiao, G. D. Zhou, S. Ranjan, W. Hou, X. Zhou, Y. Zhao, S. A. T. Redfern and Y. N. Zhou, *Nano Lett.*, **2019**, DOI: 10.1021/acs.nanolett.9b02b83.
73 Q. Xia and J. J. Yang, *Nat. Mater.*, 2019, **18**, 309-
74 F. Hussain, M. Imran, R.M. Arif Khalil, M. A. Sattar, N. A. Niaz, A. M. Rana, M. Ismail, E. A. Khera, U. Rasheed, F. Mumtaz, T. Javed and S. Kim, Vacuum, 2019, **168**, 108842.
75 H. J. Monkhorst, J. D. Pack, *Phys. Rev. B.*, 1976, **13**, 5188-5192.

Graphical Abstract

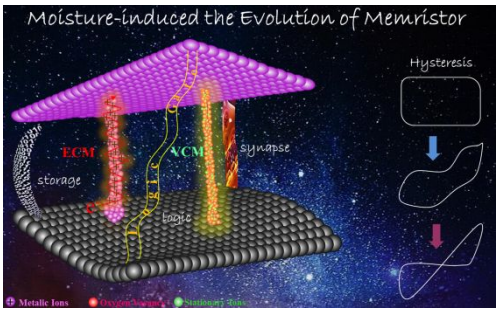

★ Evolution map of the memristor from pure capacitive state to resistive switching state is discovered.